GEOPHYSICS, VOL. 87, NO. 3 (MAY-JUNE 2022); P. IM67–IM80, 13 FIGS., 2 TABLES.
10.1190/GEO2021-0340.1

DOI:10.1190/geo2021-0340.1

Geologic-time-based interpolation of borehole data for building high-resolution models: Methods and applications

Zhengfa Bi[1], Xinming Wu[1], Yaxin Li[1], Shangsheng Yan[1], Sibo Zhang[2], and Hongjie Si[2]

ABSTRACT

Integrating borehole data into a uniformly sampled grid is an essential but challenging task for seismic data processing and reservoir characterization. We propose an efficient geologic-time-based interpolation method to build subsurface models where the structures are consistent with the seismic structures and the vertical resolution of model properties is as high as well-log records. Based on a seismic image, we first compute a relative geologic time (RGT) volume that provides an implicit map of all the geologic structures in the seismic image. We then construct an interpolated model from borehole data by following constant RGT values (each one corresponds to a same geologic layer), and thus obtain a high-resolution model honoring both seismic structures and well-log values. Such a model could provide a low-frequency control for a deep learning or conventional inversion method to estimate reservoir properties, or it can be used as a reliable initial background model to improve the performance of full-waveform inversion. We use both synthetic and field data examples to demonstrate the effectiveness of our method even when reservoir properties are only observed at sparsely scattered locations. In comparison to the existing approaches, our method can produce a more geologically consistent subsurface model which can be used as a better initial model for a deep learning method to estimate a refined rock-property model from seismic data.

INTRODUCTION

Integrating borehole data into a uniformly sampled seismic grid has become increasingly significant in recent years as oil exploration shifts to the development of existing fields that usually have many wells. Borehole data typically provide high-resolution and accurate property measurements near the well sites, but they might not offer a reliable spatial description of lateral variations of the subsurface. In contrast with sparse borehole observations, seismic data provide relatively dense but indirect measurements of subsurface acoustic properties, in which the lateral changes of seismic amplitudes across the entire volume can be transformed into variations of rock properties. However, it is challenging to model lateral changes of subsurface properties from the areal amplitude distribution because seismic data are inherently band-limited and noise-contaminated (Doyen, 1988; Hansen et al., 2008).

State-of-the-art approaches achieve integration of well logs and seismic data and enlarge the coverage of borehole data through seismic inversion (Cooke and Schneider, 1983; Oldenburg et al., 1983; Chi et al., 1984; Zhang and Castagna, 2011). Seismic inversion is the process that converts seismic traces into reservoir properties (such as the density shown in Figure 1a or the velocity shown in Figure 1b), providing highly detailed estimates of well logs even away from the boreholes. The solution of the seismic inversion is useful for a quantitative study of reservoir characterization when the low-frequency information that typically depicts large structural variations can be properly compensated by other means, such as the construction of a background model from well data.

A simple strategy to close the gap of the missing low-frequency information between the borehole and seismic data is to perform the lateral interpolation of well-log control over the entire area of interest. Most interpolation-based methods are driven by some measure of spatial distances between the seismic image samples

Manuscript received by the Editor 24 May 2021; revised manuscript received 2 December 2021; published ahead of production 24 January 2022; published online 10 March 2022.
[1]School of Earth and Space Sciences, University of Science and Technology of China, Hefei, 230026, China and Mengcheng National Geophysical Observatory, University of Science and Technology of China, Hefei, 230026, China. E-mail: zfbi@mail.ustc.edu.cn; xinmwu@ustc.edu.cn (corresponding author); yxli2017@mail.ustc.edu.cn; ssyan33@mail.ustc.edu.cn.
[2]Huawei Technologies Co. Ltd., Cloud EI Product Department, Xi'an 710077, China. E-mail: zhangsibo1@huawei.com; sihongjie@huawei.com.

and measured rock properties to weigh the influence of each well log. However, a completely distance-based routine might not correctly capture geologic structures, but they produce redundant artifacts and noisy features in the interpolated field.

Cokriging methods (Doyen, 1988; Xu et al., 1992) can be used to complete borehole data through a set of attributes and a covariance model computed from the available well logs. However, because a large number of data samples are required to derive an appropriate covariance model, it can be relatively expensive and even impractical to use when more than one attribute is involved. In addition, these methods are based on a fundamental assumption that data correlations depend on only distance and direction in physical space; however, this is not always the case when large structural variations occur.

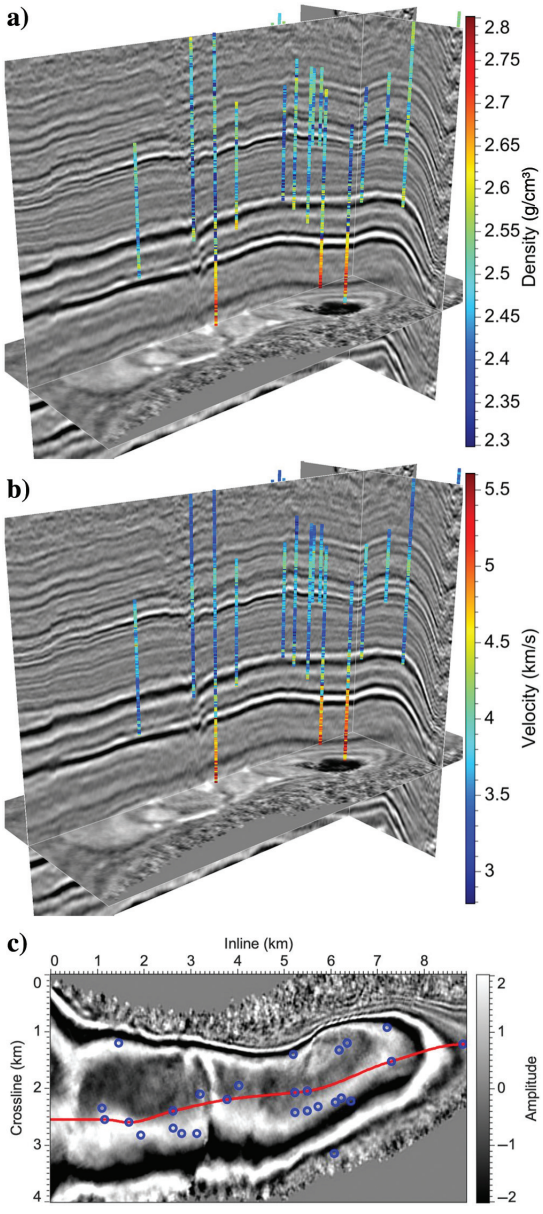

Figure 1. From (a) a 3D seismic volume and the sparsely scattered borehole data of (b) density and (c) velocity, we randomly extract a slice image along the path (the red line) passing through eight logs. Circles on (c) denote all of the well locations overlaid on a depth slice of seismic volume shown in (a).

Considerably more progress has been made to infer borehole measurements away from the well locations through other attributes computed from seismic data, which allows including additional constraints (Hampson et al., 2001; Hansen et al., 2008; Pedersen-Tatalovic et al., 2008). Although these methods provide effective ways to integrate seismic data and borehole measurements, the reflectors and other structures in the seismic image are not consistently honored and fully used to guide the interpolation of reservoir properties. This usually leads to an inaccurate interpolated model when the seismic images suffer from large variations of structures or low signal-to-noise ratio (S/N).

The missing low-frequency components of seismic images can be reliably compensated from well-log interpolation driven by a gross-layer model that includes a few horizon surfaces. In these methods, the interpolation is guided not only by the spatial distances of seismic and borehole data but also by the seismic horizons that cross multiple well logs. The seismic horizon can be extracted by manual picking or many automatic surface tracking methods (Fomel, 2002, 2010; Marfurt, 2006; Wu and Caumon, 2017), which is currently an active area of research. However, the reservoir properties located on the existing horizon surfaces can be accurately estimated, but the interpolated field might not correctly resolve others among these horizons. In addition, any picking errors on the horizon surfaces would be scattered into the interpolated field, which would significantly deteriorate the quality of the subsurface model construction.

A class of approaches (Hale, 2009, 2010; Karimi et al., 2017) has been developed to consider the structural information extracted from an image volume and represented by structure tensors as a guide to globally spreading the borehole measurements. By using such an image-guided scheme, the resulting interpolated field is consistent with the local orientations of the seismic reflectors, which drastically improves the lateral accuracy of the propagation and reduces the uncertainties of the estimates. However, when only a few well logs are available, the seismic image is noisy, or large variations of structures occur, deriving the structural features directly from the image volume might run the risk of misrepresenting geology. To solve this problem, Wu (2017) introduces prior identification of faults and horizons and then removes them from seismic and borehole data, such that seismic reflectors and borehole measurements corresponding to the same geologic layer can be horizontally aligned in an unfaulted and flattened space. The subsurface property model in this unfaulted and flattened space can be computed as a sequence of 2D horizontal interpolations of borehole data. However, it could be still difficult and even impractical to precisely compute the mappings that perfectly flatten an image volume with relatively complex structures, and these residual flattening mappings would scatter the errors into the horizontally interpolated field.

More recently, machine learning has gained significant popularity because it is capable of dealing with complex nonlinear problems and is compatible with multiple attributes as inputs. Many approaches have been proposed (Liu and Liu, 1998; Trappe and Hellmich, 2000; Hampson et al., 2001; Herrera et al., 2006) to use a neural network in the estimation of well-log properties from different seismic attributes. However, to train the network well, the learning-based methods often require a tremendous amount of labeled data that are never available in real data applications.

In this study, we present an alternative to these methods for well-log interpolation to fully honor the structural features represented in the seismic image. Instead of directly using the seismic image as a guide to enlarging the borehole data coverage, we extract the structural information by computing a relative geologic time (RGT) volume from the image volume. Such an RGT volume can be computed by interpolating from interpreted seismic horizons (Zeng et al., 1998a, 1998b), unwrapping seismic phase (Stark, 2003; Wu and Zhong, 2012), optimally fitting seismic structures (Wu and Fomel, 2018), or deep learning methods (Geng et al., 2020; Bi et al., 2021). The RGT volume can be considered as a scalar field that implicitly represents all of the structural and stratigraphic features, and therefore can be used to guide well-log interpolation to build subsurface models that conform to seismic structures.

Our RGT-based interpolation introduces new features that overcome some limitations of the existing methods: It honors lateral variations of geology such as complexly faulted and folded deposits embedded in the RGT model and can be robust against noise when constructing interpolated fields. A similar approach also has been used to estimate rock properties along with certain stratigraphic intervals through a layered model obtained from a global seismic interpretation (Luquet et al., 2016), in which the kriging and cokriging are adapted to supervise such a process and improve the lateral accuracy of the interpolation. By contrast, we apply a mathematical routine to look for a relation between the rock properties and the corresponding RGTs, in which the influence of each measured property on a single seismic sample is determined by the inverse square of spatial distances. Such a relation is implicitly embedded in the RGT space for the optimum prediction away from the borehole sites by smearing the borehole data along the same geologic layer represented by an RGT isotime. Thus, it allows obtaining a reliable property model with high vertical resolution and lateral consistency even in the presence of relatively large structural variations from vertical or deviated well logs. This structurally consistent initial background model, together with seismic data, can be further fed into a deep learning or seismic inversion method to correct the interpolation errors and improve the spatial description of rock properties by capturing the subtle variations from amplitudes.

Both the synthetic and real data examples are used to determine the ability of our method to construct a rock-property model that laterally matches the seismic structures and vertically shares the high resolution of the well log. Our method has shown superior performance to the existing methods, particularly for the cases of complex geology, a low-quality seismic image, and significantly sparse well control; thus, it has general applicability.

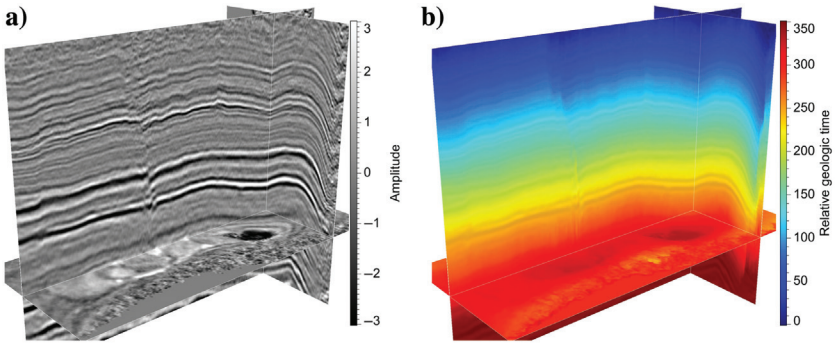

Figure 2. (a) A 3D seismic image and (b) corresponding RGT volume that is computed by using local slopes of seismic reflections and multigrid correlations of the seismic traces.

RGT

The concept of RGT was first presented and then extended by Stark (2003, 2004, 2005, 2006) and is closely related to seismic horizons that are assumed to be consistent with geologically synchronous surfaces. An RGT volume (Figure 2a) is a volumetric attribute containing a dense set of horizon surfaces, in which each sample is assigned to a geologic relative time corresponding to the reflection amplitude in the seismic volume (Figure 2a). This enables an RGT volume to store geometric relations of all types of geologic structures. For example, an RGT image (Figure 3b) with spatial dimensions identical to a seismic image (Figure 3a) can be used to look for the horizons that we wish to extract by following the set of constant RGT contours (Figure 3c). If the RGT

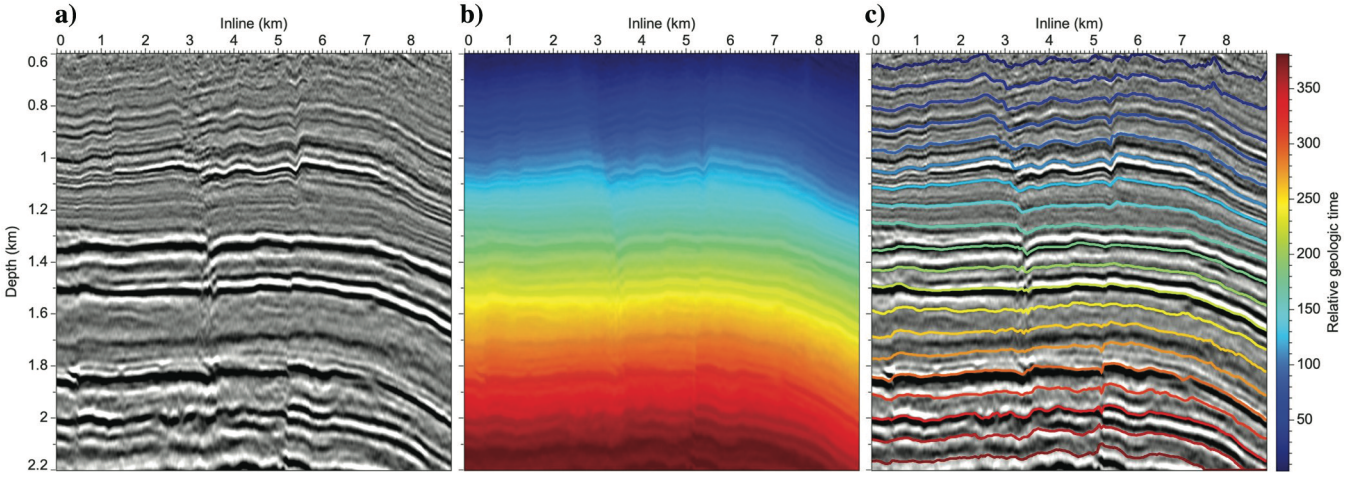

Figure 3. (a) A seismic image and (b) an RGT image extracted from Figure 2a and 2b, respectively. In an RGT image, we can find (c) the seismic horizons that we wish to extract by following the set of constant RGT contours.

DOI:10.1190/geo2021-0340.1

value can be found for every seismic sample, we can extract a horizon for each sample in a seismic image, and thus obtain all seismic horizons represented in a seismic image. In addition to horizons, additional structures such as faults, unconformities, and channels also can be represented by continuous or discontinuous features in the RGT model. Thus, an RGT volume is very useful for building subsurface structural and stratigraphic models, allowing interpreters to better understand the geology of interest to quantify reservoir properties and reveal depositional environments. RGT has been widely used and has shown great promise in many applications including horizon extraction (Fomel, 2010; Lomask et al., 2011; Wu and Zhong, 2012; Wu and Hale, 2015), sedimentologic interpretation (Hongliu et al., 2012), stratigraphic interpretation (Alliez et al., 2007; Karimi and Fomel, 2015; Lacaze et al., 2017), well-log data prediction (Bader et al., 2018), and geologic body detection (Prazuck et al., 2015).

The existing methods for computing RGT volumes can be generally divided into four categories. The first category is to manually pick or automatically track several reference horizons and then assign an RGT value to each horizon. To obtain an overall RGT volume, the values elsewhere can be calculated by using the interpolation algorithm with the known horizons for control.

In the methods of the second category, an RGT volume is computed from seismic attributes of reflector dips (Lomask et al., 2006; Parks, 2010; Luo and Hale, 2013; Karimi and Fomel, 2015) or seismic normal vectors that are perpendicular to local seismic amplitude reflectors at every image sample. The RGT volumes estimated by using these methods are more accurate for revealing local structural features in comparison to those interpolated from several discrete horizons. Instead of using seismic normal vectors, the methods in the third category (Stark, 2003, 2004, 2006; Wu and Zhong, 2012) are proposed to compute an RGT volume with high resolution, by unwrapping a related seismic instantaneous phase computed from seismic volume.

More recently, deep learning has received great attention because of its representational power for highly complex nonlinear relations and has been implemented in a variety of geophysical problems. In the fourth category of methods, Geng et al. (2020) and Bi et al. (2021) demonstrate that a form of U-shaped neural network architecture, originally designed for image classification tasks, can be successfully purposed for estimating RGT volume with excellent results.

To estimate an RGT volume (Figure 2b) from the seismic image (Figure 2a), we first extract as many horizons as possible through manual picking or through an automatic reflector tracking method, and then interpolate them into an RGT volume by assigning a constant RGT along each horizon surface. Whichever tracking method is used (Wu and Fomel, 2018), at least one control point is required, located on the horizon we wish to extract for initializing a surface passing through this point. Although the initial horizon is typically not aligned with the geologic structures, it is iteratively corrected in a least-squares system, such that the horizon slopes conform to the seismic reflectors. However, the horizon interpretation constrained by local slopes alone is insufficient for correctly tracking the structures across the discontinuities such as faults or coherent noise, because the slopes only carry the information of local orientations of laterally continuous reflectors. To solve this issue, Wu and Fomel (2018) introduce an extra constraint of multigrid slopes computed by using dynamic time warping to correlate seismic traces within multiple laterally coarse grids. These coarse-grid slopes are of high importance for guiding the algorithm to consistently track reflections significantly dislocated by faults or other discontinuous structures. Therefore, the horizon surface is estimated in the least-squares sense by simultaneously approximating the local slopes of the laterally continuous reflectors and the multigrid slopes of multigrid trace corrections. A combination of the two constraints contributes to the reliable computation of a sequence boundary or a horizon surface complicated by faults or coherent noise, which leads to an accurate estimation of RGT volume.

METHODOLOGY

Figure 1a and 1b displays a 3D real seismic volume and 27 velocity and density well logs in Teapot Dome data set, respectively (Anderson, 2009). Although there are hundreds of wells available along with the seismic data, we choose 27 logs by discarding the wells whose density or velocity logs are missing. Before building subsurface models, we enable those 27 well logs to match the seismic data, which are already converted to the depth domain.

In this section, we first introduce an RGT-based interpolation method to produce a geologically consistent subsurface model with high resolution from the seismic image and 27 borehole measurements. Then, by using the solution of RGT-based interpolation as the low-frequency control, we further apply a deep learning method to recover the high-resolution reservoir properties that honor the subtle seismic structures.

Borehole data interpolation

In general, the scattered borehole data can be represented by K log property samples:

$$\mathcal{F} = \{f_1, f_2, f_3, \ldots, f_k, \ldots, f_K\}, \tag{1}$$

where $f_k \in \mathbb{R}$ is the measurement of the reservoir property. The corresponding space coordinates $\mathbf{x}_k \in \mathbb{R}^n$ of the samples can be written as follows:

$$\mathcal{X} = \{\mathbf{x}_1, \mathbf{x}_2, \mathbf{x}_3, \ldots, \mathbf{x}_k, \ldots, \mathbf{x}_K\}. \tag{2}$$

The log properties and the corresponding space coordinates can be represented by a well L that consists of $\mathcal{K}$ known borehole data samples

$$L = \{(\mathbf{x}_1, f_1), (\mathbf{x}_2, f_2), \ldots, (\mathbf{x}_k, f_k), \ldots, (\mathbf{x}_K, f_K)\}. \tag{3}$$

The borehole data samples are usually sparsely scattered in space without any geometric structures and might not be exactly located on a uniformly sampled seismic grid. The well-log interpolation aims to use the known borehole data samples in $\mathcal{K}$ to approximate a mapping function $q(\mathbf{x})$ that spreads the log properties away from the well sites, such that $q(\mathbf{x}_k) = f_k$. We propose an RGT-based interpolation to enhance this producer, in which the interpolated values can accurately follow the geologic structures that are included in an RGT volume without any unfaulting or flattening process. Instead of horizontally aligning the well logs in a seismic unfaulted and flattened space (Wu, 2017), we find an implicit representation of the well data in the RGT space to introduce structure-related constraints in the interpolated field. Because all of the structural information is implicitly represented in the RGT volume, the well-log interpolation can be

performed only in terms of the horizontal distance within the same geologic layer that is indicated by an RGT isotime. This enables our method to robustly and reliably spread the borehole data into the entire image volume and obtain a high-resolution model that honors both the seismic structures and borehole measurements.

RGT-based interpolation

We assume that there are N well logs in an exploration survey, and each well log L_i consists of $\mathcal{K}_i$ borehole data samples

$$L_i = \{(\mathbf{x}_{1,i}, f_{1,i}), (\mathbf{x}_{2,i}, f_{2,i}), \ldots, (\mathbf{x}_{k,i}, f_{k,i}), \ldots, (\mathbf{x}_{K_i,i}, f_{K_i,i})\}, \tag{4}$$

where the sample $(\mathbf{x}_{k,i}, f_{k,i})$ is located at $\mathbf{x}_{k,i}$ and i ranges from 1 to N. With prior identification of the interpolation accuracy, we resample the raw borehole data into the corresponding interpolated sampled grid with a vertical resolution as high as or less than the well logs:

$$\hat{L}_i = \{(\hat{\mathbf{x}}_{1,i}, \hat{f}_{1,i}), (\hat{\mathbf{x}}_{2,i}, \hat{f}_{2,i}), \ldots, (\hat{\mathbf{x}}_{k,i}, \hat{f}_{k,i}), \ldots, (\hat{\mathbf{x}}_{\hat{K}_i,i}, \hat{f}_{\hat{K}_i,i})\}, \tag{5}$$

in which we preserve a borehole data sample with the median value of rock properties in each vertical grid when there exist multiple samples. Correspondingly, the RGT volume is required to be constructed in the same interpolated sampled grid to be consistent with the well-log resolution, such that we can look for a time value $\tau_{k,i}$ to correspond to each resampled borehole record $\hat{\mathbf{x}}_{k,i}$ in the RGT space. This RGT volume is used to transform each well log i from the physical space into the RGT space as

$$L_{k,i} = \{(\tau_{1,i}, \hat{f}_{1,i}), (\tau_{2,i}, \hat{f}_{2,i}), \ldots, (\tau_{k,i}, \hat{f}_{k,i}), \ldots, (\tau_{\hat{K}_i,i}, \hat{f}_{\hat{K}_i,i})\}, \tag{6}$$

which enables the interpolation to be implemented along with certain stratigraphic intervals with similar RGTs.

For each well log, we approximate a relation function between the RGT values and the log properties by using linear interpolation, such that $p_i(\tau_{k,i}) = \hat{f}_{k,i}$. This function provides borehole measurements even at the grid samples in which the properties are never observed. Thus, we define a weighting function $h_i(\tau)$ to highlight the reservoir properties recorded at this well log. This function has a maximum value of one at the grid samples in which the properties are observed, and a minimum value of zero for the others in which the borehole data are missing.

To control the interpolated value changes within the layer, we introduce distance-related weights by using radial base functions (RBFs) that rescale the contributions of every borehole record, in which the importance depends on its horizontal Euclidean distance from the interpolated grid sample. There are many possible options for choosing RBFs, and we choose the commonly used inverse quadratic radial function:

$$w_i(x, y) = \frac{1}{K_i} \sum_{k=1}^{K_i} \frac{1}{1 + \epsilon^2((x - x_k)^2 + (y - y_k)^2)}, \tag{7}$$

which assigns a larger weight to the borehole record near the interpolated grid sample. In this RBF, ϵ represents a radial parameter used to balance the distance-related importance of the observed well data. This hyperparameter is set to one based on prior experiments and kept fixed throughout the study to avoid the need for tuning. The scalar value one in the denominator of the equation is used to avoid the numerical error when the interpolated grid sample exactly lies on the borehole data samples.

Therefore, the interpolated property at each grid sample $\mathbf{x}$ is computed by smearing all of the borehole data along the same geologic layer by following an RGT isosurface, which can be written as follows:

$$q(x, y, \tau) = \frac{\sum_{i=1}^{N} w_i(x, y) h_i(\tau) p_i(\tau)}{\sum_{i=1}^{N} w_i(x, y) h_i(\tau)}. \tag{8}$$

The RGT-based interpolation is not limited to the fixed resolution of the seismic image and can be used to construct the subsurface model with vertical resolution less than or as high as the borehole measurements according to our prior identification of the interpolated grid. Figure 1c shows the spatial positions of the 27 well logs overlaid on a depth slice of the seismic volume (Figure 1a). We extract a seismic section, shown in Figure 4a, along the path (displayed by the red line in Figure 1c) passing through eight velocity logs. In Figure 4c–4e, we show the velocity images obtained from the RGT-based interpolation with a variety of vertical resolutions, including one, two, and four times the seismic sample rate, respectively. However, in the image-guided interpolation (Hale, 2010), which is considered as the reference method in this study, the vertical resolution is constrained to equal the input seismic sampled grid. In comparison with the results of the reference method shown in Figure 4b, our solutions appear to not only be more laterally consistent with the structures but also contain vertically clearer stratigraphic boundaries. To display greater

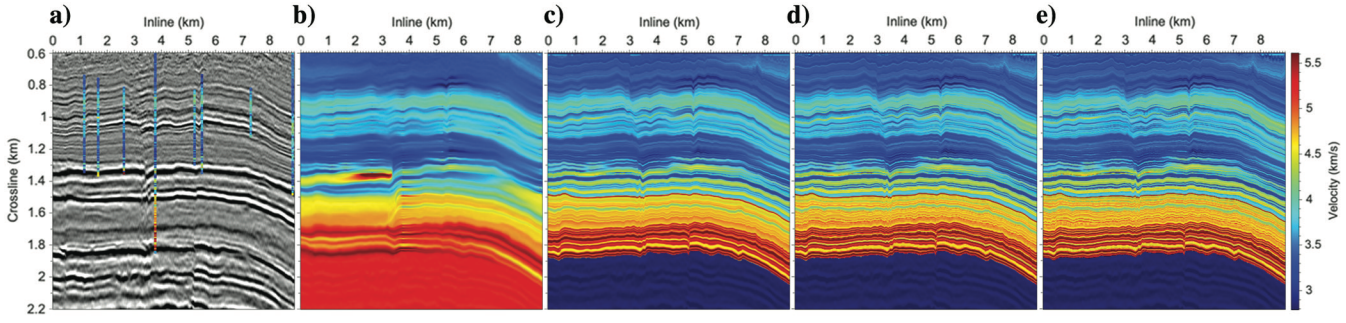

Figure 4. (a) Seismic image extracted along the path (displayed by the red line in Figure 1c) passing through the eight velocity logs. Velocity image derived by using (b) image-guided interpolation (Hale, 2010) and RGT-based interpolation with different spatial resolutions in terms of (c) one, (d) two, and (e) four times the seismic sample rate, respectively.

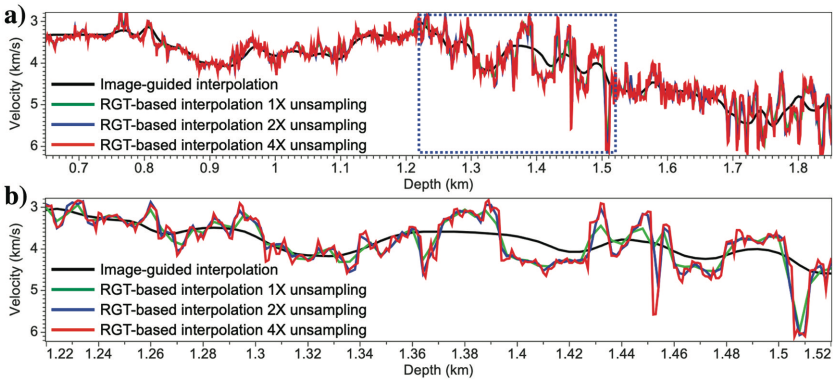

Figure 5. (a) Well logs extracted at the same position of velocity images obtained from different interpolation schemes (Figure 4b–4e) and (b) their corresponding magnified view within the blue box in shown in (a).

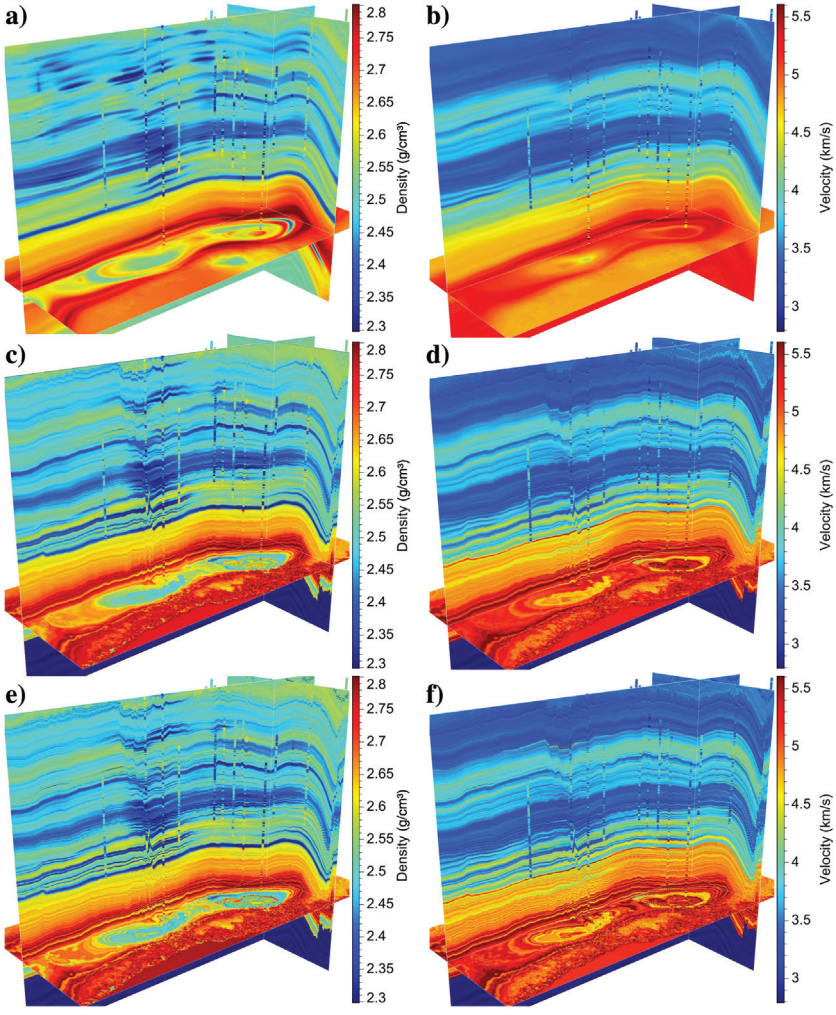

Figure 6. Compared with (a) density and (b) velocity models obtained from the image-guided method (Hale, 2010), the models (c and d) constructed by the RGT-based interpolation approach have structural features more consistent with the seismic image under the same sample rate. In addition, because the sample rate of the interpolation is not necessarily limited to the seismic image, we can further improve the vertical resolution of the models, as shown in (e and f), respectively, which have a sample rate that is four times finer.

detail, we randomly extract one velocity trace at the same position from each of four velocity images, and we display the magnified view of the traces within the blue box of Figure 5a in Figure 5b. With the denser interpolated sampled grid, the interpolated velocity traces show increasingly higher vertical accuracy, which indicates that our method fully takes advantage of the high resolution of the well log. In addition, even using the input seismic sample rate, the result of our approach appears to capture more features of velocity changes than the reference method (Figure 5).

To further demonstrate the effectiveness of the proposed method, we spread the borehole measurements of density and velocity, respectively, to the entire image volume using image-guided interpolation (Figure 6a and 6b; Hale, 2010) and RGT-based interpolation (Figure 6c and 6d). Because the sample rate of the interpolation is not necessarily limited to the seismic image grid, the vertical resolution of the interpolated model can be higher than the seismic data. For example, we show the results derived by using a sample rate four times finer than the input sample rate in Figure 6e and 6f, from which we can observe a significant improvement of the vertical resolution in comparison to the reference method (Figure 6b). To show details of these solutions, we compute two velocity traces at nine randomly chosen well sites and display them in Figure 7a–7i. As shown in Figure 7, our interpolation method not only provides more reliable low-frequency information that is consistent with the lateral variations of the structures but also achieves a comparable vertical resolution as high as the well logs. Moreover, this method without any seismic image processing can be performed more efficiently than the existing approaches that adopt an iterative optimizer to solve a large optimization problem. Using a 28-core computer, our parallel implementation of the RGT-based interpolation takes approximately 6.10 s, whereas the reference method requires approximately 4965.70 s for processing the Teapot Dome seismic volume (with size $401 \times 357 \times 161$). However, the interpolated values at the well sites might not fully honor the observed well data, which generates the necessity of further correcting interpolation errors to reveal subtle variations from the seismic amplitudes.

Seismic inversion

Seismic inversion is a process of converting the seismic amplitudes into the subsurface properties, providing highly detailed estimates of the borehole measurements away from the well sites. However, in comparison with the well logs, seismic data typically have limited bandwidth due to the geometry of the recording layout, the sample rate, source energy, and frequency. The solution

DOI:10.1190/geo2021-0340.1

of the seismic inversion process can be useful in a quantitative study of reservoir characterization when the information gap between the zero and the low end of the frequency bandwidth among boreholes can be reasonably filled.

This problem can be addressed by building a realistic initial background model that correctly compensates for the band-limited nature of seismic data. To properly model the low-frequency information, one should compensate for not only the amplitude spectrum but also the phase spectrum represented by the lateral continuity of the surface horizons. Therefore, this initial model needs to not only consistently track the geologic structures but also conform to the observed well logs, such that the optimization of the seismic inversion can avoid local minima to obtain a reliable full-bandwidth solution.

For achieving these two requirements, we adopt our RGT-based interpolation followed by a low-pass filter to build a geologically consistent initial model. With such a reliable initial model as the low-frequency trend control, structural patterns in the image volume can be properly included in the final solution of the seismic inversion.

Learning-based seismic inversion

In this section, we use a deep learning method to perform the seismic inversion that is typically considered as a highly ill-posed optimization problem. Deep learning (LeCun et al., 2015; Goodfellow et al., 2016) is a data-driven system that learns a mapping function to make predictions from inputs, according to example data or past experiences through iterative optimization. It has shown great ability in capturing high-level and complex nonlinear relations from data without any prior knowledge of physical equations or mathematical theories. More recently, deep learning in practice has achieved excellent performance in numerous geophysical problems, such as channel interpretation (Pham et al., 2019; Yao et al., 2019), salt detection (Gramstad and Nickel, 2018; Sen et al., 2020; Shi et al., 2019), fault interpretation (Xiong et al., 2018; Wu et al., 2019), and horizon interpretation (Sen et al., 2020).

With the seismic volume and borehole data, we perform a supervised deep learning method to spread reservoir properties away from the well sites. We use a simple 1D convolutional neural network (CNN) to trace-wise predict an impedance model from the seismic image, in which we introduce the low-frequency constraint of the initial model computed by the RGT-based interpolation. The seismic volume (Figure 2a) is a part of the freely available Teapot Dome data set, which contains 401 (vertical) × 357 (inline) × 161 (crossline) samples, from which we estimate the corresponding RGT volume (Figure 2b). The impedance data are obtained from the density and velocity well logs, which have been sampled to be consistent with the depth-migrated seismic image. We perform the proposed RGT-based interpolation to obtain an impedance volume, which is smoothed by a low-pass filter to build an initial model as low-frequency trend control of the impedance inversion.

Figure 8 shows the network architecture that we use to perform the seismic inversion. This network sequentially consists of a convolution layer and a stack of residual blocks followed by a convolutional layer that makes predictions of impedance trace by trace. From the input seismic traces and the low-frequency constraint, the first convolutional layer with a kernel size of 5 × 5 computes 16 feature vectors, which are then passed into the parametric rectified linear unit (PReLU) activate function (He et al., 2015) and the instance normalization (IN). The activated feature vectors are fed into a stack of four sequentially linked residual modules (He et al., 2016). The architecture of every residual module is displayed in Figure 8. It consists of three successive convolutional layers in a form of bottleneck design implemented by 16 convolutional filters with sizes of 1×1, 3×3, and 1×1, respectively. Such a framework has been widely used in constructing CNNs to improve the performance and speed up the calculation, in which the two 1×1 convolutional layers are responsible for increasing and then decreasing channels and the middle depth-wise layer is used to handle four times as many feature vectors. In addition, the shortcut connection over the two ends of the convolutional layers is used to formulate the module as a residual learning function, which is helpful for gradient backpropagation in training the network. Following these residual modules, the final learning unit is a 1×1 convolutional layer responsible for predicting impedance sequences. The architecture of the CNN model used in this study is quite simple, but it is sufficient to apply to the problem of rock property estimation.

With the measured impedance well logs as targets, it is straightforward to implement the seismic inversion by training a supervised learning network, in which the inputs consist of the seismic traces and the low-frequency prior constraints, and the output is the target properties. In training the network, we randomly intercept the impedance well logs into the patches with the fixed size of 80 borehole data samples and extract the corresponding input data, while preserving the full length of well logs in validation.

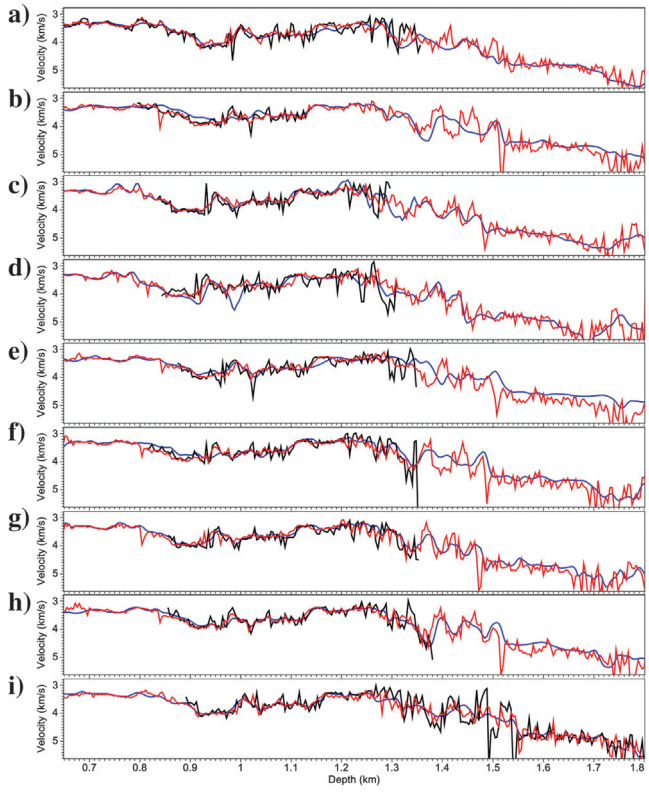

Figure 7. Comparisons of the observed borehole data (black) and the corresponding well logs estimated by using image-guided interpolation (blue) and our RGT-based interpolation method (red). Results at the nine validation logs (a-i): compared to the sonic logs estimated by using the image-guided interpolation (blue), the ones obtained by using our RGT-based interpolation method (red) match the ground truth or observed ones (black) better.

DOI:10.1190/geo2021-0340.1

To stabilize the training, we perform a normalization scheme for both the input data and target sequences. In this normalization, we compute the means and the standard deviations of the overall volume (including seismic volume and initial impedance model) and the entire well logs. The input and target sequences are subtracted by using the corresponding means and then divided by the corresponding standard deviations to obtain the normalized sequences. At the same time, we record the mean and standard deviation of the measured well logs, such that we are able to recover the correct log properties when inferring the impedances away from the well sites. In training the network, we formulate the normalized data in batches, and the batch size is set to be four. Because estimating impedance sequences from seismic traces with or without initial sequences is a classic regression problem, we choose the commonly used mean square error (MSE) as the loss function:

$$\mathcal{L}_{\mathrm{MSE}} = \frac{1}{N}\sum_{i=1}^{n} w_i \cdot (y_i - y_i^p)^2, \tag{9}$$

where y_i and y_i^p represent the ith sample of predictions and target properties, respectively; N denotes the number of all the samples; and w_i represents a binary mask that is equal to one at the well-log samples and zero elsewhere. We use the Adam optimizer with an adaptive step length to speed up the training. The initial learning rate is set to be 0.01, which gradually reduces when the predefined metric performance has stopped improving. The epoch number is set to be 501 and all of the input data are processed in an epoch. The parameters of the convolutional kernels are initialized by using the Kaiming method (He et al., 2015) to avoid gradient exploding or vanishing across hidden layers.

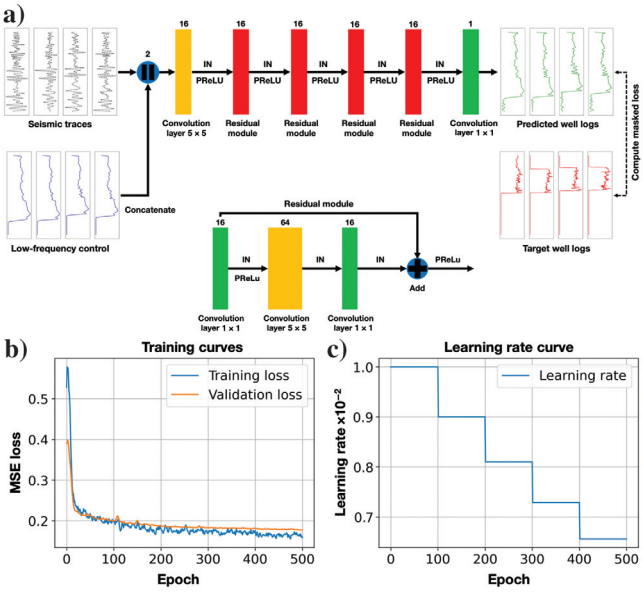

Figure 8. (a) Proposed sequential network consisting of a convolution layer and a stack of residual blocks to make predictions of subsurface property trace by trace. It is worth noting that we mask out the loss being performed to prevent the accumulation of gradients in which no valid borehole measurement exists. (b) The loss curves in training and validation steps. During the training process, the learning rate is adaptively adjusted, as shown in (c).

The loss functions (MSE) for both training and validation converge to less than 0.2 after 500 epochs (Figure 8a) when the optimization stops (Figure 8b). The loss curves shown in Figure 8a indicate an appropriate end to the training because more epochs produce insignificant performance gains. To evaluate the training performance, we use four seismic traces in the validation data set to estimate the corresponding impedances. The validation data set contains the other four well logs, kept separate from the interpolation and training processes as the blind test, to fully prove the improvement of the final inverted results.

Figure 9a–9c shows the predicted impedances (the black lines) overlaid on the observed well data (the red lines), respectively, and Figure 9d–9f shows the corresponding cross validations of the blind validation log highlighted by the blue box. In the cross validations, the predicted impedances are placed on the vertical axis and the targets on the horizontal axis. Thus, the black diagonal lines represent how the correct answer should appear, whereas the red lines are the linear regression results through the inverted impedances.

We show the impedances obtained from the RGT-based interpolation and the crossing validation of the blind well in Figure 9a and 9b, respectively. However, we can still observe some oscillations and mismatches in the validation logs. Although the interpolated impedances do not fully follow the observed well data, they can be used as a reliable low-frequency control for the following deep learning method to stabilize the prediction and compensate for the interpolation errors based on the seismic amplitudes. As shown in Figure 9b, compared with the interpolated impedances, the impedances predicted from the network visually match the measurements better, and the crossing regression result shows a higher correlation (Figure 9f) as it is closer to a diagonal line that represents perfect consistency. These observations demonstrate the further improvement of the estimated impedances introduced by our CNN. By contrast, we apply the initial model computed by the image-guided interpolation to train the same CNN and show its predicted results on the four validation logs and the crossing-validation solution in Figure 9c and 9g, respectively. Although the estimated impedances generally show consistent variations with the observed well data, it is still difficult to accurately capture the measured impedances that rapidly vary with depth. We also show the results derived by training the network without any low-frequency constraint in Figure 9d and 9h, in which the trained CNN is not sufficient to present a complex and spatially varying relationship between the seismic data and the borehole measurements. It is obvious that using a proper initial model as low-frequency control is significant for the network to predict a much more stable and reliable solution.

To further verify the effectiveness of the workflow, we use the same network trained by using the two different prior models and without any low-frequency constraint to propagate the measured impedances over the entire image volume. By using the RGT-based interpolated prior model (Figure 9i) that is aligned with seismic horizons, seismic structural patterns can be robustly included in the final predicted impedances (Figure 9j). Compared to the predicted model of the CNN trained with the reference method (Figure 9k), our solution shows not only laterally more consistent features but also vertically thin geologic layers by tracking the relatively large structural changes of the reflections. However, with the input of only the seismic data, the learning-based seismic inversion yields a noisy impedance model (Figure 9l) with many unreasonable discontinuities, and it fails to produce stable and

DOI:10.1190/geo2021-0340.1

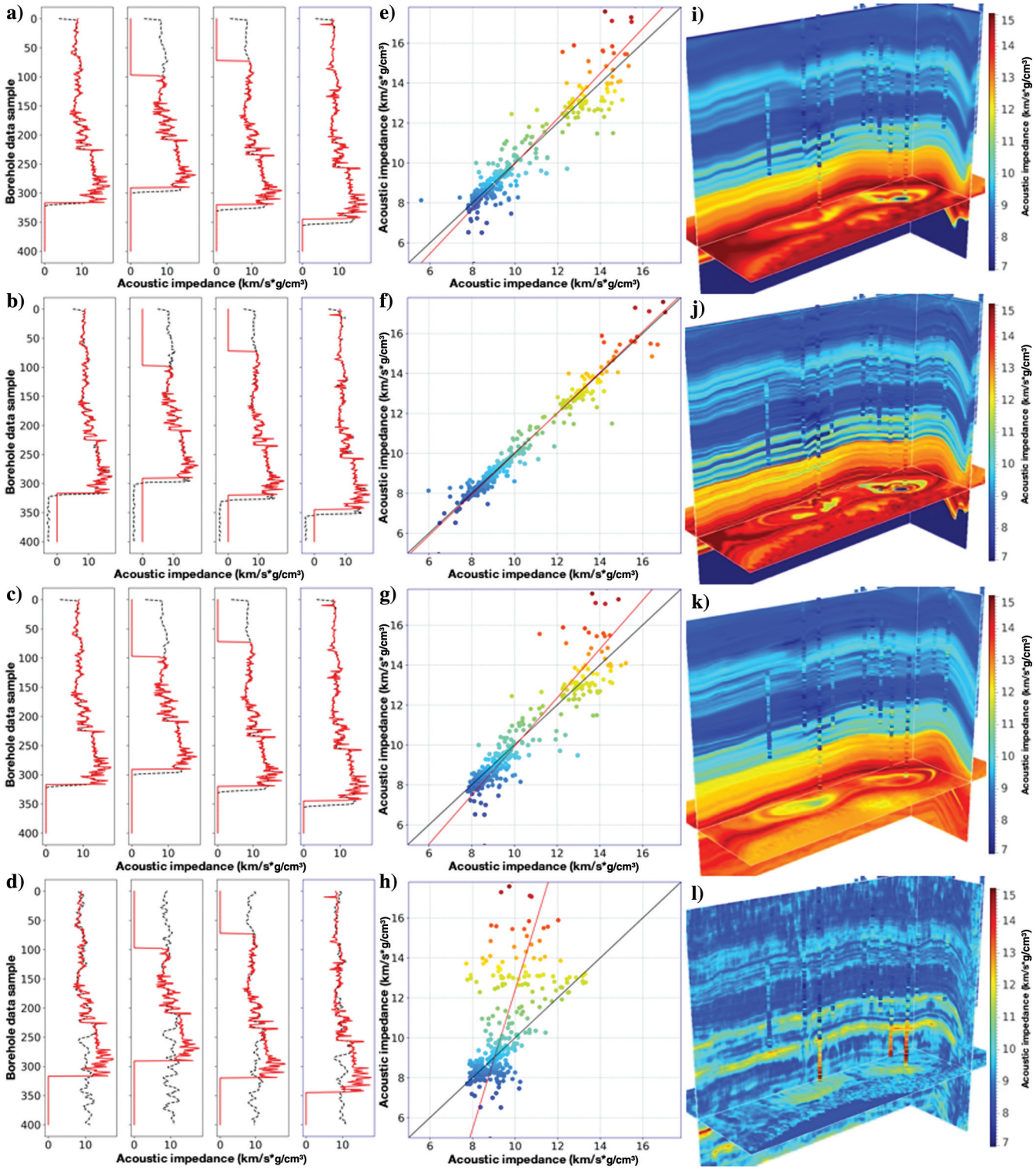

Figure 9. Well logs (the red lines) overlaid on the impedances (the black lines) estimated by using (a) the RGT-based interpolation, (b) deep learning with RGT-based interpolation model, (c) deep learning with image-guided interpolation model, and (d) the deep learning method without any low-frequency control, and (e-h) the corresponding cross validation of the blind well log (the blue box), respectively. (i-l) The impedance models that correspond to these methods, obtained by propagating the well data over the entire volume, respectively.

geologically consistent predictions. This also can be illustrated by the trace overlap and crossing validation of the observed and predicted impedances (Figure 9f and 9h), in which the predictions match better if a reliable initial model is available. Table 1 displays a quantitative comparison of the normalized MSE of the estimated impedances at the four validation logs. We observe that the predictions obtained from the CNN trained with the RGT-based interpolation model show the highest accuracy (or smallest MSE) at each of the logs.

APPLICATION

Deviated well data application

Not limited to vertical well logs, the proposed method also can be adopted to successfully estimate a rock-property model from any complexly deviated or horizontal log. To demonstrate, we provide a synthetic data example with 17 deviated well logs that have different extension directions and deviation angles, in which we randomly choose four logs for the validation and the rest for training the network to predict impedances over the entire volume. We adopt a workflow (Wu et al., 2020) to automatically create a synthetic seismic volume (Figure 10a) by sequentially adding realistic folding, dipping, faulting, and noise in an initial layered model. By reproducing all of the structures in this seismic volume, we obtain the corresponding RGT model (Figure 10b) and the ground truth of the impedance model (Figure 10c). It is worth noting that the faults are highlighted by the red color and overlaid within the seismic volume in Figure 10a.

As shown in Figure 10d, we use the RGT-based interpolation to construct a high-resolution model that vertically matches the measured impedances and laterally honors the variations of the structures. To further demonstrate the power of our approach, we display the impedances along the two chronostratigraphic surfaces that are extracted by tracking the constant RGT isotime in Figure 10e and 10f, respectively. Figure 10g shows a comparison of the model computed from the reference method. Correspondingly, Figure 10h and 10i displays the impedance distributions over the same chronostratigraphic surfaces.

In the reference method, the structure tensors honoring local structural orientations might not precisely track the lateral discontinuities of the seismic reflectors, and the interpolated impedances within the same layer would be different on opposite sides of the faults (Figure 10h and 10i), which creates the risk of misrepresenting the geology. By contrast, our approach appears to be not only more robust to seismic noise but also structurally consistent, because it correctly recovers thin layers (highlighted by the black arrows in Figure 10d and 10g), which are vertically subtle but may laterally extend over a large area. In addition, it also better follows relatively large structural changes, which can be verified by the consistent rock properties over the chronostratigraphic surfaces that are dislocated across the faults.

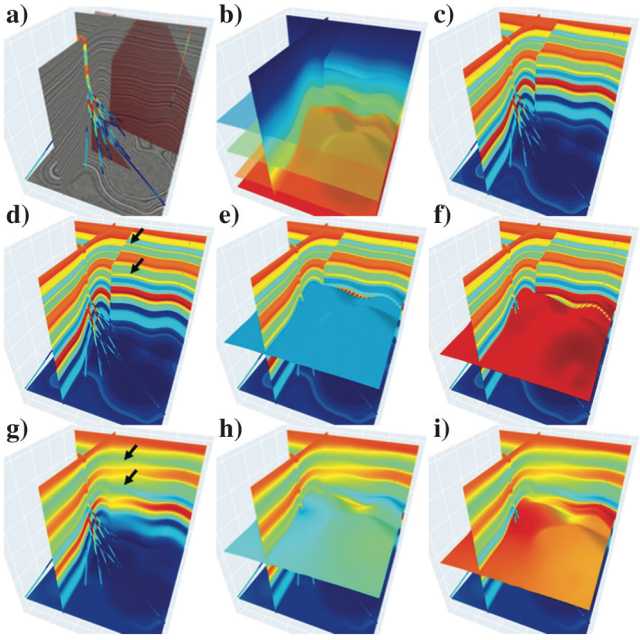

Figure 10. (a) Synthetic data example with the 17 deviated well logs and the noisy seismic volume complicated by the two faults are colored by the red surfaces. When creating seismic volume, we also obtain (b) the corresponding RGT model and (c) the ground truth of the impedance model. We first adopt the RGT-based interpolation to compute (d) an impedance model, and then extract the impedances along two chronostratigraphic surfaces, as shown in (f and g), respectively. For comparison, we display the model derived by the reference method and show its impedance distributions over the same chronostratigraphic surfaces in (h and i), respectively.

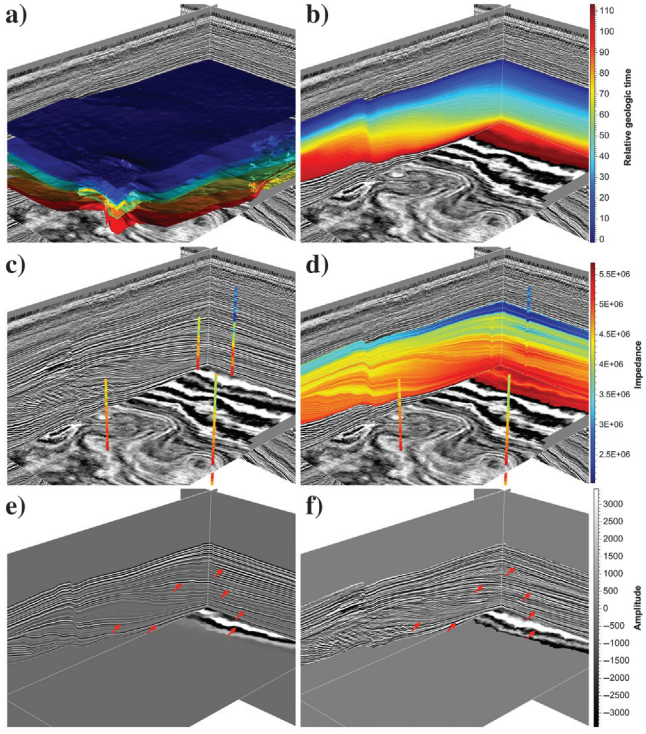

Figure 11. From the seven horizons provided along with the 3D seismic image shown in (a), we interpolate (b) a 3D RGT volume, which is further used to compute (c) an interpolation of the four impedance logs to obtain (d) a high-resolution impedance model. From the interpolated impedance model, we further calculate (e) a synthetic seismic image, which is consistent with (f) the real seismic image, especially those events denoted by the red arrows.

F03 block data application

We use a 3D data volume from the Netherlands, North Sea (F03 block in the Dutch sector) from the TNO and the Dutch government to test the proposed approach. Figure 11 shows the seismic volume along with seven interpreted horizons (Figure 11a) and the four available well logs (Figure 11c). Because of significantly sparse wells and complicated structures, constructing a reliable subsurface model is highly challenging for many existing well-log interpolation methods. Using the seven horizons, we compute an RGT volume (Figure 11b) which fully honors the horizon interpretation and offers important structural information that implicitly depicts the spatial variation of rock properties. This RGT model is used to drive the well-log interpolation within the geologic layers and obtain a high-resolution and structurally consistent impedance model, as shown in Figure 11d. For demonstrating the quality of this result, we compute the corresponding reflectivity model from the interpolated impedances, which is then convolved with a Ricker wavelet to generate a synthetic seismic volume. As shown in Figure 11e, this synthetic seismic image is generally consistent with the seismic structures in the real image volume, especially for those reflection events within the unconformity zone denoted by the red arrows in Figure 11f.

To better control the structural variations at the bottom of the image volume, we additionally compute a seismic horizon by using an automatic horizon-tracking method (Wu and Fomel, 2018), which is combined with the seven interpreted horizons to construct an accurate RGT model. Using only the existing sparse wells and the RGT model, we implement the RGT-based interpolation followed by a low-pass filter to compute a starting background model, which serves as reliable low-frequency trend control in the deep learning method. The initial impedance model (Figure 12a),

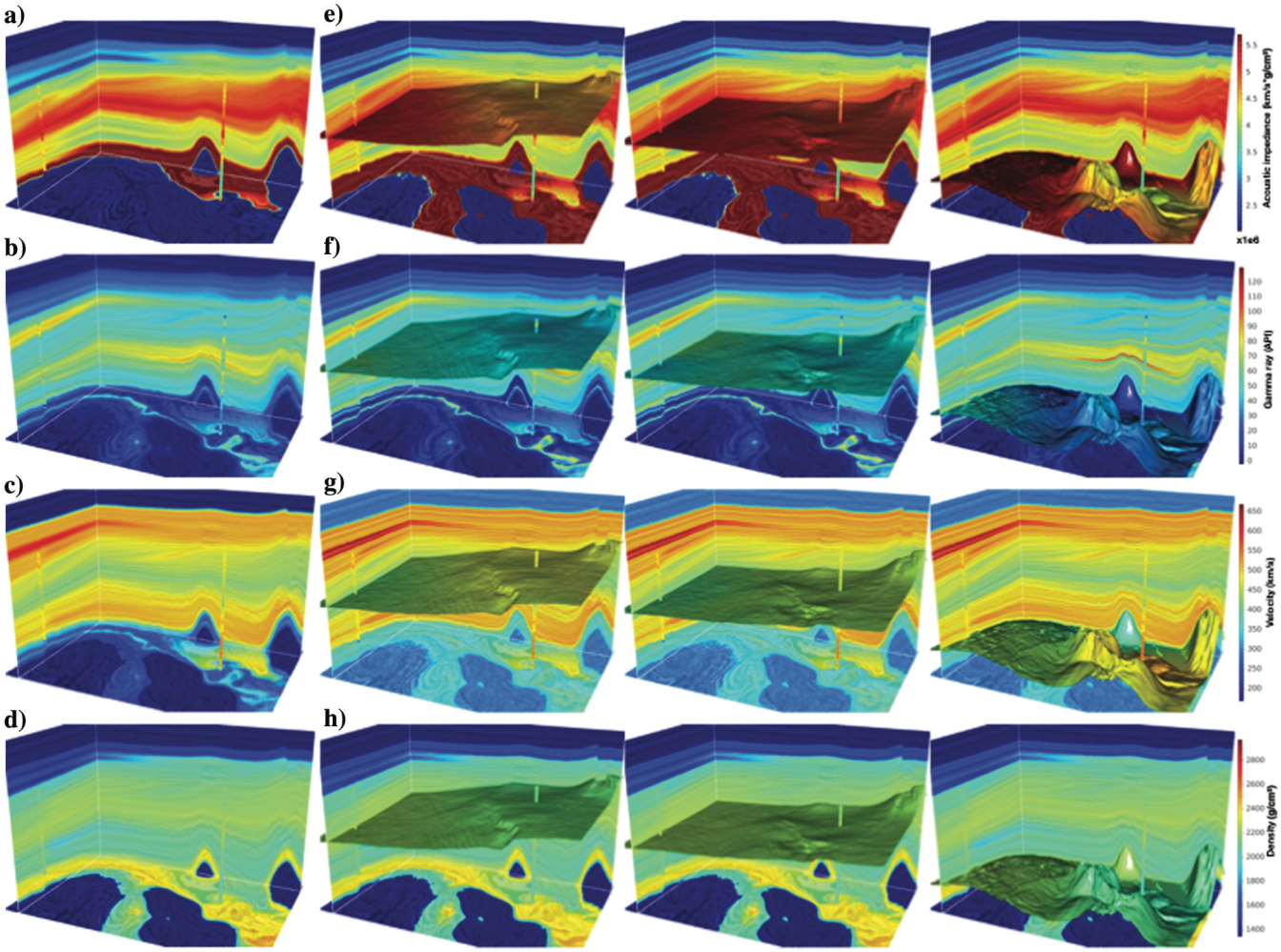

Figure 12. We adopt the RGT-based interpolation to obtain the initial background models of (a) acoustic impedance, (b) gamma ray, (c) velocity, and (d) density, which are used as low-frequency constraints in the deep learning method to further improve accuracy. To demonstrate the structural consistency of the CNN predictions, we show the rock properties along the three interpreted horizons overlaid on the corresponding predicted model from (e) to (h), respectively.

together with the seismic data, is passed through the network (Figure 8) to capture detailed spatial variations of the rock properties and correct interpolation errors based on the seismic amplitudes. To evaluate the performance of our network, we use three logs for training, whereas the remaining one is used for the validation log. We display the impedance distributions over two of the interpolated horizon surfaces and one automatically tracked horizon surface in Figure 12e, wherein they are overlaid in the predicted volume. We find that the estimated impedances are generally consistent along the horizon surfaces, and the obtained impedance model conforms with the seismic structural pattern, even for the boundary of the sigmoidal configuration and the complexly overlying reflectors. In addition, taking advantage of the high resolution of the well logs, our method can accurately recover subtle, vertically thin layers that extend in a large area from the initial background model, which is still challenging but of great importance in reservoir characterization. As shown in Figure 13a, the predicted impedances match the measured values well, including the validation well log (highlighted by the blue box) that is excluded from the prediction and interpolation. This observation is also supported by the cross validation of the blind test well shown in Figure 13e, in which the impedances predicted by the CNN present high correlations with the well-log impedances.

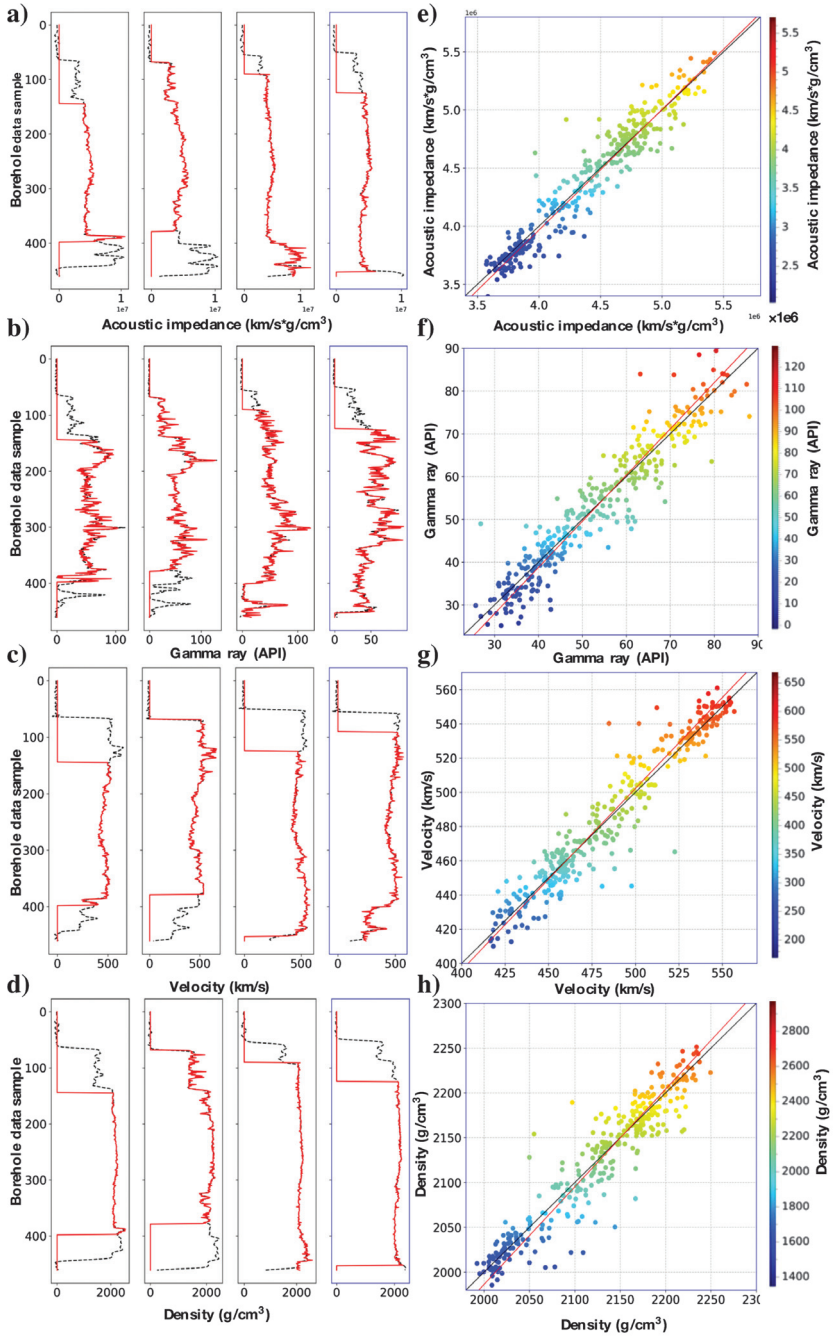

Figure 13. The predicted traces (the black lines) of (a) acoustic impedance, (b) gamma ray, (c) velocity, and (d) density, which are all overlaid on the corresponding well data (the red lines), and (e-h) the related crossing validation on the blind well log (the blue box), respectively.

In addition to the acoustic impedance, our approach also can be used to build other types of rock-property models that are geologically consistent with the seismic structures. By following the same workflow, we use our RGT-based interpolation followed by a low-pass filter to build the prior background models from the well-log data of gamma ray, velocity, and density, shown in Figure 12b to 12d, respectively. We show the corresponding models predicted from the network in Figure 12f to 12h, which not only precisely recover the vertically subtle features of the thin layers but also well match the lateral changes of the seismic reflections. In addition, these observations can be supported by the consistent distributions of the estimated values along the two horizon surfaces within the unconformity zone and the one at the bottom of the image volume. Figure 12b–12d shows that the predicted values match the measured values well in the three training logs and the remaining validation log. The corresponding cross validations at the blind test well (Figure 12f–12h) also show substantial agreement between the measured and predicted rock properties. Table 1 shows a quantitative comparison of the normalized MSE of the predicted rock properties using the deep learning method with and without the prior background model. When training logs are limited and the rock properties vary rapidly, the CNN model trained using seismic data alone fails to yield reliable rock-property estimations. By contrast, although trained using only three logs, the results of the CNN model trained with the prior model and seismic data exhibit significantly smaller MSE at the validation log, which demonstrates that such a prior model is helpful for the CNN to yield stable predictions.

Table 1. The comparison of the networks trained with the RGT-based and image-guided interpolation models and without any low-frequency prior model, respectively, in the Teapot Dome field and F03 block data applications.

Teapot Dome data set

Prior model	RGT-based interpolation	Without a prior model	Image-guided interpolation
Log 1	**0.087**	0.923	0.187
Log 2	**0.083**	1.212	0.266
Log 3	**0.088**	1.459	0.133
Log 4	**0.117**	1.322	0.213

F03 block data set

Prior model	RGT-based interpolation	Without a prior model
Impedance	**0.149**	2.151
Gamma ray	**0.073**	1.341
Velocity log	**0.078**	1.918
Density log	**0.147**	0.294

For the used quality metric (normalized MSE), smaller value indicates better performance, and the best result is highlighted in bold.

CONCLUSION

We propose an RGT-based interpolation to construct a geologically consistent model from sparsely scattered well data and provide enough accurate low-frequency control to be further exploited in a deep learning or seismic inversion method for improving accuracy. From a 3D seismic image, we first compute an RGT model as an implicit representation of all the structures by using local slopes of seismic reflections and multigrid correlations. Based on this RGT model, we then build an interpolated field in which the structural pattern is consistent with the seismic image and the spatial resolution can be as high as the measured well data. Although using only a few wells, it still produces an accurate subsurface model that is structurally consistent with the seismic image while matching the measured borehole data well, and thus significantly enhances the estimation of the rock properties. In addition, without any iterative optimizer used for solving a large nonlinear equation, such as the image-guided interpolation (Hale, 2010), our RGT-based method is performed efficiently, allowing us to look for the well logs that have relatively large deviations from the others. For this task, we first exclude a well log from the interpolation and then compare the interpolated properties to the observed data at the same well site, in which their difference indicates how compatible this well log is among the other borehole data. Moreover, the proposed method also can assist in the identification of regions where the geology is either insufficiently represented in the seismic image or different from that sampled by the wells. This information about geologic changes is essential for many related reservoir characterization studies and helps decide on the need and value of further appraisal.

To estimate an RGT volume, we first extract horizons through an automatic or manual picking method and then assign a constant RGT isotime on each horizon surface. With the known time values, we can interpolate the RGTs elsewhere and obtain a full model. By this means, we can flexibly integrate the prior geologic knowledge of the horizon interpretation into the RGT computation. Although the obtained RGT volume can strictly honor the horizon surfaces and consistently follow the lateral variations of reflectors, it is still challenging to capture the local structures among the horizons. The structure-related errors can be scattered into the interpolated field, which degrades the quality of the subsequent optimized modeling in the seismic inversion. To further improve our approach, we need to offer an accurate RGT estimation by fully honoring the geologic structures, which is actually what we are planning to do in future work.

We use two field data applications to determine the ability of the proposed approach in constructing a geologically consistent subsurface model with high vertical resolution. To verify that our approach is not limited to the vertical logs, we additionally present a synthetic data example with complicatedly deviated well logs and successfully construct a reliable subsurface model that generally matches the ground truth. More accurate and robust computation of rock properties gives more confidence for well placement and reservoir characterization.

ACKNOWLEDGMENTS

This research was financially supported by the National Science Foundation of China under grant no. 42050104 and Huawei Cloud Computing Technologies Co. Ltd. The field seismic and well-log data in Figure 1 are provided by the Rocky Mountain Oilfield Test Center. The field data set in Figure 11 is provided by dGB Earth Sciences B.V. through OpendTect.

DATA AND MATERIALS AVAILABILITY

Data associated with this research are available and can be obtained by contacting the corresponding author.

REFERENCES

Alliez, P., D. Cohen-Steiner, Y. Tong, and M. Desbrun, 2007, Voronoi-based variational reconstruction of unoriented point sets: Symposium on Geometry Processing, 39–48.

Anderson, T., 2009, History of geologic investigations and oil operations at Teapot Dome: Presented at the Annual Convention, AAPG.

Bader, S., K. Spikes, and S. Fomel, 2018, Missing well-log data prediction using Bayesian approach in the relative-geologic time domain: 88th Annual International Meeting, SEG, Expanded Abstracts, 804–808, doi: 10.1190/segam2018-2997278.1.

Bi, Z., X. Wu, Z. Geng, and H. Li, 2021, Deep relative geologic time: A deep learning method for simultaneously interpreting 3D seismic horizons and faults: Journal of Geophysical Research: Solid Earth, **126**, no. 9, 1–24, doi: 10.1029/2021JB021882.

Chi, C.-Y., J. M. Mendel, and D. Hampson, 1984, A computationally fast approach to maximum-likelihood deconvolution: Geophysics, **49**, 550–565, doi: 10.1190/1.1441690.

Cooke, D. A., and W. A. Schneider, 1983, Generalized linear inversion of reflection seismic data: Geophysics, **48**, 665–676, doi: 10.1190/1.1441497.

Doyen, P. M., 1988, Porosity from seismic data: A geostatistical approach: Geophysics, **53**, 1263–1275, doi: 10.1190/1.1442404.

Fomel, S., 2002, Applications of plane-wave destruction filters: Geophysics, **67**, 1946–1960, doi: 10.1190/1.1527095.

Fomel, S., 2010, Predictive painting of 3D seismic volumes: Geophysics, **75**, no. 4, A25–A30, doi: 10.1190/1.3453847.

Geng, Z., X. Wu, Y. Shi, and S. Fomel, 2020, Deep learning for relative geologic time and seismic horizons: Geophysics, **85**, no. 4, WA87–WA100, doi: 10.1190/geo2019-0252.1.

Goodfellow, I., Y. Bengio, and A. Courville, 2016, Deep learning: MIT Press.
Gramstad, O., and M. Nickel, 2018, Automated interpretation of top and base salt using deep convolutional networks: 88th Annual International Meeting, SEG, Expanded Abstracts, 1956–1960, doi: 10.1190/segam2018-2996306.1.
Hale, D., 2009, Image-guided blended neighbor interpolation of scattered data: 79th Annual International Meeting, SEG, Expanded Abstracts, 1127–1131, doi: 10.1190/1.3255050.
Hale, D., 2010, Image-guided 3D interpolation of borehole data: 80th Annual International Meeting, SEG, Expanded Abstracts, 1266–1270, doi: 10.1190/1.3513074.
Hampson, D. P., J. S. Schuelke, and J. A. Quirein, 2001, Use of multiattribute transforms to predict log properties from seismic data: Geophysics, **66**, 220–236, doi: 10.1190/1.1444899.
Hansen, T. M., K. Mosegaard, R. Pedersen-Tatalovic, A. Uldall, and N. L. Jacobsen, 2008, Attribute-guided well-log interpolation applied to low-frequency impedance estimation: Geophysics, **73**, no. 6, R83–R95, doi: 10.1190/1.2996302.
He, K., X. Zhang, S. Ren, and J. Sun, 2015, Delving deep into rectifiers: Surpassing human-level performance on ImageNet classification: Proceedings of the IEEE International Conference on Computer Vision, 1026–1034.
He, K., X. Zhang, S. Ren, and J. Sun, 2016, Deep residual learning for image recognition: Proceedings of the IEEE Conference on Computer Vision and Pattern Recognition, 770–778.
Herrera, V. M., B. Russell, and A. Flores, 2006, Neural networks in reservoir characterization: The Leading Edge, **25**, 402–411, doi: 10.1190/1.2193208.
Hongliu, Z., Z. Xiaomin, Z. Rukai, and Q. Zhang, 2012, Guidelines for seismic sedimentologic study in non-marine postrift basins: Petroleum Exploration and Development, **39**, 295–304, doi: 10.1016/S1876-3804(12)60045-7.
Karimi, P., and S. Fomel, 2015, Stratigraphic coordinates: A coordinate system tailored to seismic interpretation: Geophysical Prospecting, **63**, 1246–1255, doi: 10.1111/1365-2478.12224.
Karimi, P., S. Fomel, and R. Zhang, 2017, Creating detailed subsurface models using predictive image-guided well-log interpolation: Interpretation, **5**, no. 3, T279–T285, doi: 10.1190/INT-2016-0051.1.
Lacaze, S., B. Durot, A. Devilliers, and F. Pauget, 2017, Comprehensive seismic interpretation to enhance stratigraphy and faults: Proceedings of the 15th International Congress of the Brazilian Geophysical Society & EXPOGEF, 1429–1432.
LeCun, Y., Y. Bengio, and G. Hinton, 2015, Deep learning: Nature, **521**, 436–444, doi: 10.1038/nature14539.
Liu, Z., and J. Liu, 1998, Seismic-controlled nonlinear extrapolation of well parameters using neural networks: Geophysics, **63**, 2035–2041, doi: 10.1190/1.1444496.
Lomask, J., A. Guitton, S. Fomel, J. Claerbout, and A. A. Valenciano, 2006, Flattening without picking: Geophysics, **71**, no. 4, P13–P20, doi: 10.1190/1.2210848.
Lomask, J. M., J. M. Francis, W. S. Kowalik, and Y. Altobi, 2011, System and method for perturbing an initial horizon-picking solution to follow local features of a volume: U. S. Patent App. 13/193,300.
Luo, S., and D. Hale, 2013, Unfaulting and unfolding 3D seismic images: Geophysics, **78**, no. 4, O45–O56, doi: 10.1190/geo2012-0350.1.
Luquet, B., T. Valding, F. Cubizolle, and N. Daynac, 2016, New technique for rock physics prediction based on the seismic interpretation: 78th Annual International Conference and Exhibition, EAGE, Extended Abstracts, doi: 10.3997/2214-4609.201601229.
Marfurt, K. J., 2006, Robust estimates of 3D reflector dip and azimuth: Geophysics, **71**, no. 4, P29–P40, doi: 10.1190/1.2213049.
Oldenburg, D., T. Scheuer, and S. Levy, 1983, Recovery of the acoustic impedance from reflection seismograms: Geophysics, **48**, 1318–1337, doi: 10.1190/1.1441413.
Parks, D., 2010, Seismic image flattening as a linear inverse problem: M.S. thesis, Colorado School of Mines.
Pedersen-Tatalovic, R., A. Uldall, N. L. Jacobsen, T. M. Hansen, and K. Mosegaard, 2008, Event-based low-frequency impedance modeling using well logs and seismic attributes: The Leading Edge, **27**, 592–603, doi: 10.1190/1.2919576.
Pham, N., S. Fomel, and D. Dunlap, 2019, Automatic channel detection using deep learning: Interpretation, **7**, no. 3, SE43–SE50, doi: 10.1190/INT-2018-0202.1.
Prazuck, C., B. Durot, V. Sava Jol, and S. Lacaze, 2015, Interpretation of complex geo-bodies using a relative geological time model: Exmouth sub-basin, Australia: 85th Annual International Meeting, SEG, Expanded Abstracts, 1643–1647, doi: 10.1190/segam2015-5866995.1.
Sen, S., S. Kainkaryam, C. Ong, and A. Sharma, 2020, SaltNet: A production-scale deep learning pipeline for automated salt model building: The Leading Edge, **39**, 195–203, doi: 10.1190/tle39030195.1.
Shi, Y., X. Wu, and S. Fomel, 2019, SaltSeg: Automatic 3D salt segmentation using a deep convolutional neural network: Interpretation, **7**, no. 3, SE113–SE122, doi: 10.1190/INT-2018-0235.1.
Stark, T. J., 2003, Unwrapping instantaneous phase to generate a relative geologic time volume: 73rd Annual International Meeting, SEG, Expanded Abstracts, 1707–1710, doi: 10.1190/1.1844072.
Stark, T. J., 2004, Relative geologic time (age) volumes-relating every seismic sample to a geologically reasonable horizon: The Leading Edge, **23**, 928–932, doi: 10.1190/1.1803505.
Stark, T. J., 2005, Generating a seismic Wheeler volume: 75th Annual International Meeting, SEG, Expanded Abstracts, 782–785, doi: 10.1190/segam2012-1177.1.
Stark, T. J., 2006, Visualization techniques for enhancing stratigraphic inferences from 3D seismic data volumes: First Break, **24**, doi: 10.3997/1365-2397.24.1094.26926.
Trappe, H., and C. Hellmich, 2000, Using neural networks to predict porosity thickness from 3D seismic data: First Break, **18**, 377–384, doi: 10.1046/j.1365-2397.2000.00091.x.
Wu, X., 2017, Building 3D subsurface models conforming to seismic structural and stratigraphic features: Geophysics, **82**, no. 3, IM21–IM30, doi: 10.1190/geo2016-0255.1.
Wu, X., and G. Caumon, 2017, Simultaneous multiple well-seismic ties using flattened synthetic and real seismograms: Geophysics, **82**, no. 1, IM13–IM20, doi: 10.1190/geo2016-0295.1.
Wu, X., and S. Fomel, 2018, Least-squares horizons with local slopes and multigrid correlations: Geophysics, **83**, no. 4, IM29–IM40, doi: 10.1190/geo2017-0830.1.
Wu, X., Z. Geng, Y. Shi, N. Pham, S. Fomel, and G. Caumon, 2020, Building realistic structure models to train convolutional neural networks for seismic structural interpretation: Geophysics, **85**, no. 4, WA27–WA39, doi: 10.1190/geo2019-0375.1.
Wu, X., and D. Hale, 2015, Horizon volumes with interpreted constraints: Geophysics, **80**, no. 2, IM21–IM33, doi: 10.1190/geo2014-0212.1.
Wu, X., L. Liang, Y. Shi, and S. Fomel, 2019, Faultseg3D: Using synthetic data sets to train an end-to-end convolutional neural network for 3D seismic fault segmentation: Geophysics, **84**, no. 3, IM35–IM45, doi: 10.1190/geo2018-0646.1.
Wu, X., and G. Zhong, 2012, Generating a relative geologic time volume by 3D graph-cut phase unwrapping method with horizon and unconformity constraints: Geophysics, **77**, no. 4, O21–O34, doi: 10.1190/geo2011-0351.1.
Xiong, W., X. Ji, Y. Ma, Y. Wang, N. M. AlBinHassan, M. N. Ali, and Y. Luo, 2018, Seismic fault detection with convolutional neural network: Geophysics, **83**, no. 5, O97–O103, doi: 10.1190/geo2017-0666.1.
Xu, W., T. Tran, R. Srivastava, and A. G. Journel, 1992, Integrating seismic data in reservoir modeling: The collocated cokriging alternative: Presented at the Annual Technical Conference and Exhibition, SPE.
Yao, X., M. Zhang, M. Sun, C. Zhou, Y. Yi, and G. Hu, 2019, A 3D channel body interpretation via multiple attributes and supervoxel graph cut: Interpretation, **7**, no. 4, T739–T749, doi: 10.1190/INT-2018-0158.1.
Zeng, H., M. M. Backus, K. T. Barrow, and N. Tyler, 1998a, Stratal slicing — Part 1: Realistic 3-D seismic model: Geophysics, **63**, 502–513, doi: 10.1190/1.1444351.
Zeng, H., S. C. Henry, and J. P. Riola, 1998b, Strata slicing — Part 2: Real 3-D seismic data: Geophysics, **63**, 514–522, doi: 10.1190/1.1444352.
Zhang, R., and J. Castagna, 2011, Seismic sparse-layer reflectivity inversion using basis pursuit decomposition: Geophysics, **76**, no. 6, R147–R158, doi: 10.1190/geo2011-0103.1.

Biographies and photographs of the authors are not available.